Defect-rich O-incorporated 1T-MoS$_2$ nanosheets for remarkably enhanced visible-light photocatalytic H$_2$ evolution over CdS: The impact of enriched defects

Xiao-Hong Zhang[a], Nan Li[a], Jiaojiao Wu[a], Yan-Zhen Zheng[b,*], Xia Tao[a,b,*]

[a] State Key Laboratory of Organic-Inorganic Composites, Beijing University of Chemical Technology, Beijing 100029, China
[b] Research Center of the Ministry of Education for High Gravity Engineering & Technology, Beijing University of Chemical Technology, Beijing 100029, China

ARTICLE INFO

ABSTRACT

Structure and phase engineering in low-cost and earth-abundant MoS$_2$ materials have been widely explored in catalytic domains. Designing MoS$_2$ nanostructures associated with the number of catalytically active edge sites is of particular importance for obtaining an effective HER photocatalytic system. We herein report hydrothermal-synthesized defect-rich O-incorporated 1T-MoS$_2$ nanosheets (denoted as DRM), and their implementation as cocatalysts to form photocatalytic heterostructure with CdS nanorods (denoted as DRM-C). For comparison, defect-free O-incorporated 1T-MoS$_2$ nanosheets (denoted as DFM) and corresponding heterostructure i.e. DFM-C were simultaneously synthesized. A carefully comparative study on DRM and DFM demonstrates that the DRM cocatalyst exhibits more abundant defects in the basal planes and edges, and thus leading to the higher density of active sites beneficial to the photocatalytic HER. As a result, the optimized 20 wt% DRM-C exhibits an extraordinary visible-light ($\lambda > 420$ nm) photocatalytic H$_2$ production rate of 132.4 mmol h^{-1} g^{-1}, obviously higher than that of 20 wt% DFM-C (102.1 mmol h^{-1} g^{-1}). Interestingly, such an impressive activity of 20 wt% DRM-C is demonstrated to be superior to that of pure CdS (20.0 mmol h^{-1} g^{-1}) and conventional Pt/CdS (89.0 mmol h^{-1} g^{-1}). To the best of our knowledge, this DRM-C photocatalyst shows the advanced visible-light-driven HER performance among reported MoS$_2$/CdS composites.

1. Introduction

Due to emerged energy crisis and global environmental awareness, the conversion of solar energy into chemical fuels via photocatalytic water splitting using semiconductors as catalysts has attracted significant attention [1–4]. As a promising semiconductor photocatalyst, CdS has a suitable band gap (about 2.4 eV) and a correct conduction-band edge potential (more negative than the reduction potential of H$_2$O/H$_2$) for capturing visible light and splitting water [5–9]. However, bare CdS shows the extremely low activity for photocatalytic hydrogen evolution reaction (HER) due to its rapid photogenerated electron-hole recombination and lack of active sites for proton reduction [10]. Integration of cocatalyst on CdS semiconductor material has proven to be an effective way for suppressing electron-hole recombination and accelerating photocatalytic HER [11]. The commonly-used HER cocatalysts include noble metals such as Pt, Au and Pd, though their practical applications are largely restricted due to the low abundance and high cost [11–13].

Over the past few years, enormous efforts have been devoted to exploring alternatives to noble metal cocatalysts, including transition metal carbides [14], nitrides [15], borides [16], sulfides [17–20], phosphides [21,22], selenides [23], and phosphosulfides [24]. As a typical layered transition metal disulfides, MoS$_2$ consisting of three atom layers (S-Mo-S) stacking together via weak van der Waals interaction has been extensively investigated and demonstrated to be in a position to be utilized as cocatalyst for CdS due to its earth-abundant composition, high performance and explicit catalytic mechanism. However, as demonstrated by experimental and theoretical studies, conventional MoS$_2$ materials possess limited active sites and poor conductivity and thus restrict their potential ability to compete the state-of-the-art catalysts in photocatalytic systems [25–29]. To address these issues, various strategies such as defect engineering [30–34], phase engineering [35], preferential exposure of active facets [36,37] and amorphization [38–40] have been explored, with the enhanced photocatalytic HER activities in varying degrees. Recently, some studies focus on engineering defect and/or phase structure for much enhanced photocatalytic H$_2$ evolution [41,42]. Wu's group reported a cocatalyst of defect-decorated MoS$_2$ nanoplates via a one-pot hydrothermal

method and found that the defect-rich MoS_2 shows excellent promotion of photocatalytic hydrogen over CdS [41]. Wang et al. developed the defect-rich oxygen-doped MoS_2/CdS composite via a facile hydrothermal method, which exhibits an efficient visible-light photocatalytic activity for H_2 evolution from water splitting [42]. They revealed that the defects in the MoS_2 nanosheets provide additional active S atoms on the exposed edge sites, and the incorporation of O reduces the energy barrier for H_2 evolution and increases the electric conductivity of the MoS_2 nanosheets. Apart from defects and O-incorporation as the key roles in determining the HER performance, the active sites and electronic conductivity can also be improved by phase conversion of MoS_2 i.e. from a trigonal semiconducting phase (denoted as $2H$-MoS_2) to an octahedral metallic phase (denoted as $1T$-MoS_2) (the crystal structures of 2H and 1T phases are shown in Fig. S1). As reported previously [17,43], $1T$-MoS_2 offers dense active sites containing catalytically active edges and basal planes, while the $2H$-MoS_2 only possesses the edge sites. Besides, $1T$-MoS_2 exhibits HER catalytic performance superior to that of the semiconducting 2H phase due to enhanced intrinsic catalytic activity facilitating the charge transfer kinetics [14,38]. Regrettably, the photocatalytic HER activities of $1T$-MoS_2/CdS heterostructure in several existing reports are far unsatisfactory and the usual preparation procedures associated with $1T$-MoS_2 are tedious, accompanied by high risk of using metallic lithium. In this context, to integrate all aforementioned favorable features of MoS_2, we are motivated to fabricate a high-performance MoS_2/CdS heterostructure i.e. defect-rich O-incorporated $1T$-MoS_2/CdS using facile and environment-friendly methods. Accordingly, a comparative study of defect-rich and defect-free in O-incorporated $1T$-MoS_2 to correlate the density of active sites and the corresponding photocatalytic activity is also of great importance for rational and controllable defect modulation in the overall H_2 evolution enhancement.

Herein, we report on the synthesis of structure- and phase-engineered MoS_2 nanosheets i.e. defect-rich O-incorporated $1T$-MoS_2 nanosheets (denoted as DRM) via a facile hydrothermal method. For comparison, defect-free O-incorporated $1T$-MoS_2 nanosheets (denoted as DFM) were also synthesized in parallel. Note that DRM and DFM were simply modulated by adding more and less thiourea precursor, respectively. The preparation procedures for hybrid photocatalysts obtained by integrating DRM or DFM with CdS nanorods (denoted as DRM-C and DFM-C) are schematically illustrated in Fig. 1. A comparative study on DRM-C and DFM-C demonstrates that the photocatalytic HER activity of the former is superior to that of latter, predominantly due to the higher density of active sites originated from the abundant defects. Besides, DRM-C is proven to show more merits of charge transfer and separation in comparison with DFM-C. Under an

optimized DRM/CdS ratio of 20 wt%, DRM-C achieves a remarkable enhanced visible light (λ > 420 nm) photocatalytic H_2 production rate of 132.4 mmol h^{-1} g^{-1}, far higher than that of pure CdS (20.0 mmol h^{-1} g^{-1}), 20 wt% DFM-C (102.1 mmol h^{-1} g^{-1}) and conventional Pt/CdS (89.0 mmol h^{-1} g^{-1}). To the best of our knowledge, this heterostructure photocatalyst shows the advanced visible-light-driven photocatalytic HER performance among reported MoS_2/CdS composites.

2. Experimental section

2.1. Materials synthesis

2.1.1. Preparation of DRM and DFM

For the synthesis of DRM, 1.2 g hexaammonium heptamolybdate tetrahydrate $((NH_4)_6Mo_7O_{24}\cdot4H_2O)$ and 2.2 g thiourea (NH_2CSNH_2) were dissolved in 35 mL deionized water under vigorous stirring to form a homogeneous solution. Subsequently, the solution was added into a 100 mL Teflon-lined stainless steel autoclave and maintained at 200 °C for 24 h. After cooling naturally, the black precipitate was collected by centrifugation, washed with deionized water and absolute ethanol for several times and dried at 60 °C under vacuum. For comparison, the same procedure was used to synthesize DFM only by reducing the amount of thiourea (1.1 g).

2.1.2. Preparation of CdS

CdS was fabricated as in previous research [44]. Specifically, 4.6 g cadmium chloride hemipentahydrate $(CdCl_2\cdot2.5H_2O)$ and 4.6 g NH_2CSNH_2 were added into a Teflon-lined, stainless-steel autoclave filled with ethylenediamine to 60% of its capacity (100 mL). The autoclave was sealed and heated in an oven at 160 °C for 48 h and then allowed to cool down to room temperature. The yellow precipitate was collected and washed with absolute ethanol and distilled water to remove the solvent residues.

2.1.3. Preparation of the hybrid catalysts

In order to characterize the performance of the hybrid catalysts, a series of composite photocatalysts powers were prepared. In a typical experiment, 100 mg CdS and 20 mg of as-prepared DRM or DFM were added into 30 mL of ethanol, and the mixture was sonicated and stirred for 1 h, respectively. Subsequently, the ethanol was evaporated at 80 °C to gain the target product of 20 wt% composite catalyst. Using the same method, a series of hybrid materials, including 10 wt%, 15 wt%, 25 wt% and 30 wt% DRM-C and DFM-C, were obtained by adjusting the amounts of two cocatalysts as 10, 15, 25 and 30 mg, respectively.
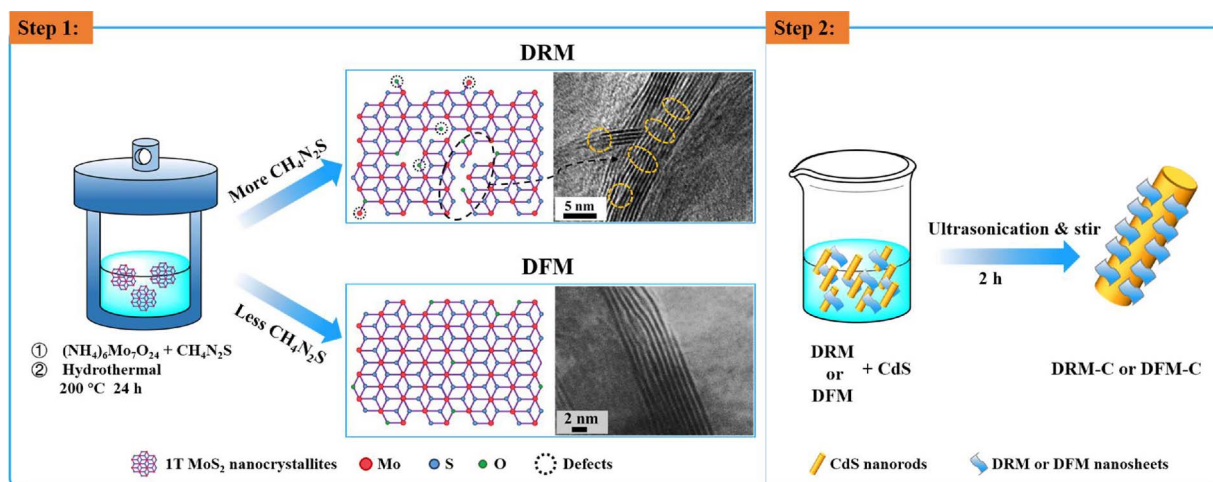

Fig. 1. Step 1: schematic illustration of the defect-controlled synthesis of DRM and DFM nanosheets through a hydrothermal technique by adding more and less thiourea precursor, respectively. Step 2: schematic illustration for the formation of DRM-C or DFM-C via facile ultrasonication and stir treatments.

2.2. Characterizations

The crystalline structure of samples was characterized by powder X-ray diffraction (XRD) using Cu Ka radiation (λ = 0.15406 nm) on a Rigaku D/max-2500 VB2 + /PC diffractometer in the 2θ range 3-90° at a scanning rate of 10°/min. The morphology of as-prepared samples was characterized by scanning electron microscopy (SEM) (JEOL JSM-6701F) and high-resolution transmission electron microscopy (HRTEM) (JEOL JEM-3010). X-ray photoelectron spectroscopy (XPS) analysis was performed on a Thermo ESCALAB250 X-ray photoelectron spectrometer using Al Ka as an X-ray source. Electron spin resonance (EPR) spectrum was acquired using a JEOL JES-FA200 X-band spectrometer. Fourier transform infrared (FTIR) spectrum was measured on a Bruker Vertex 70v spectrometer. Zeta-potentials of the samples in water were measured by a Malvern zeta analyzer (Nano-ZS 90, Malvern Instrument, UK). An energy-dispersive spectroscopy (EDS) measurement was performed with an X-ray energy dispersive spectrometer installed on a JEOL-6701F microscope. The optical property of samples was determined by using the absorption spectra recorded on a UV–vis spectrophotometer (Perkin Elmer Lambda 950 UV–vis). Photoluminescence (PL) spectra were obtained on a Hitachi F7000 with an excitation wavelength of 426 nm.

2.3. Photoelectrochemical measurements

Photoelectrochemical measurements were performed in a standard three-electrode quartz cell with a H_2SO_4 (cocatalyst system) or Na_2SO_4 (composite catalyst system) electrolyte solution, in which a saturated calomel electrode (SCE) was used as the reference electrode. As for cocatalysts, a graphite rod (Alfa Aesar, 99.9995%) and the foam nickel substrate loaded with various cocatalysts (DRM or DFM) samples were chosen as the counter electrode and the working electrodes, respectively. As for composite catalysts, a platinum wire and the composite samples (DRM-C or DFM-C) were used as the counter electrode and the working electrodes, respectively. A typical preparation procedure for the DRM or DFM based working electrodes as follows: 12 mg cocatalyst and 90 μL Nafion were dispersed in 3 mL water-ethanol solution (volume ratio of 3:1), followed by sonicating for 1 h to form a homogeneous solution. Then 10 μL the dispersion (containing 40 μg cocatalyst) was dripped onto the foam nickel substrate. A typical preparation procedure for the hybrid materials based working electrodes as follows: the suspension prepared by dispersing 10 mg DRM-C or DFM-C catalyst into a ternary solution containing 100 μL Nafion, 400 μL ethanol and 500 μL H_2O was dropped onto the pretreated indium tin oxide substrate, followed by drying at 40 °C. The on-off light photoresponse and electrochemical impedance spectroscopy (EIS) measurements were performed at the open-circuit potential, and the frequency range was fixed from 1 to 10^5 Hz. The photocurrent density-voltage (I–V) curves were measured in the bias sweep range − 1 to 1 V.

2.4. Photocatalytic H_2 evolution

The photocatalytic H_2-production experiments were performed in an outer irradiation type photoreactor (50 mL quartz glass). 2 mg CdS and a certain amount of DRM or DFM suspension in water (0.4 mg mL^{-1}) were mixed in 20 mL of an aqueous solution containing 10 vol% lactic acid. Then, the suspension was sonicated and stirred for 1 h, respectively, to obtain DRM-C or DFM-C photocatalyst. Before irradiation, the suspension was thoroughly degassed to remove air by bubbling N_2 for 30 min. During the water splitting experiment, the suspension was stirred and irradiated by a 500 W metal halide lamp (Perfect Light, Beijing), which is equipped with an optical filter (λ > 420 nm) to cut off the light in the ultraviolet region. The reaction temperature was adjusted to room temperature by a flow of cooling recycling water. The evolved gas was analyzed by a gas chromatograph (GC-TP2080, BFTP, China, TCD, nitrogen as carrier gas and TDX-01

carbon molecular sieve column). The apparent quantum yield (AQY) of photocatalysts were measured using appropriate band pass filters (420 and 600 nm, respectively) to perform the H_2 production experiments under the designated monochromic light. The AQY values were calculated using the following equation:

$$AQY(\%) = \frac{2 \times \text{number of evolved } H_2 \text{ molecules}}{\text{number of incident photons}} \times 100\%$$

3. Results and discussion

3.1. Structure and property of cocatalysts

The XRD patterns of DRM and DFM are shown in Fig. S2. Compared with the pristine MoS_2 (PDF#75-1539), the (002) peak of DFM and DRM is shifted to a lower degree 9.0°, and a second-order diffraction peak with 18.0° simultaneously appears, confirming the existence of the 1T phase in DRM and DFM. Similar phenomena have been observed in the exfoliated 1T-MoS_2 [45,46]. The phase composition and chemical bonding states of DRM and DFM were investigated by XPS. All the core level peaks of Mo 3d, O 1s and the S 2p regions in DRM and DFM have no obvious change. From the Mo 3d spectrum (Fig. 2a), peaks at around 229.5 and 232.7 eV correspond to Mo^{4+} $3d_{5/2}$ and Mo^{4+} $3d_{3/2}$ components of 2H-MoS_2, respectively [47]. Deconvolution of these peaks reveal additional peaks that are shifted to lower binding energies by ~ 0.8 eV with respect to the position of the 2H-MoS_2 peaks. Similarly, in the S 2p region of the spectra (Fig. 2b), additional S^{2-} $2p_{3/2}$ and S^{2-} $2p_{1/2}$ peaks for the 1T phase at 161.6 and 162.9 eV are found besides the known doublet peaks for the 2H phase. The parallel shift of these additional peaks to a lower binding energy suggests the formation of 1T phase, which is similar to the previous reports concerning Li-intercalated MoS_2 [48,49]. The concentration of the 1T phase in DRM and DFM samples were approximately calculated ~ 87%. The O 1s peak located at 531.6 eV (Fig. 2c) corresponds to the binding energy of oxygen in $Mo^{(IV)}O_2$ [31], thus verifying the existence of $Mo^{(IV)}$—O bonds in the DRM and DFM matrix rather than surface oxidation [33,50]. Besides, the O 1s peak located at 533.3 eV can be attributed to the adsorbed water molecules [42]. Moreover, the presence of the Mo—O bond signal (235.6 eV) in the Mo 3d spectra (Fig. 2a) also confirms the incorporation of O. Element analysis results of DRM and DFM are summarized and listed in Table S1. These results provide the direct evidence for O-incorporation in the MoS_2 lattices. According to the previous report, the oxygen incorporation in MoS_2 can effectively improve the intrinsic conductivity and reduce the energy barrier for H_2 evolution [31,42].

The SEM images (Fig. 3a and b) clearly reveal flower-like morphology of as-obtained DRM, and lateral size of the nanosheets is in the range of 200–300 nm. The corresponding TEM image (Fig. 3c) also verifies the nanosheet morphology of DRM. The HRTEM images taken from one zone in Fig. 3c are shown in Fig. 3d and e. Remarkably, the crystal fringes are discontinuous and appear many dislocations and distortions as indexed in the images, implying the existence of rich defects on the basal planes and edges. Further, these additional defects will enhance the density of active sites, which are supposed to be beneficial to HER [20]. Interplanar spacing of 0.27 nm (± 0.03 nm) can be observed from Fig. 3d, which is consistent with the d spacing of (100) planes of MoS_2. Besides, interplanar spacing from Fig. 3e was measured as 0.70 nm (± 0.03 nm), which are attributed to the d spacing of (002) planes of MoS_2. Particularly, such interlayer distance of 0.70 nm is slightly larger than the layer-to-layer of 0.61 nm in bulk MoS_2 [51], which could be reasonably deduced to the O-incorporation in the MoS_2 structure by replacing S at S sites [31,33,42]. In parallel, the TEM characterization of DFM (Fig. S3a and b) was also performed. We observed that no obvious defects or cracks appeared in the DFM structure. The interplanar spacing of about 0.7 nm (± 0.03 nm) is attributed to (002) planes of DFM.
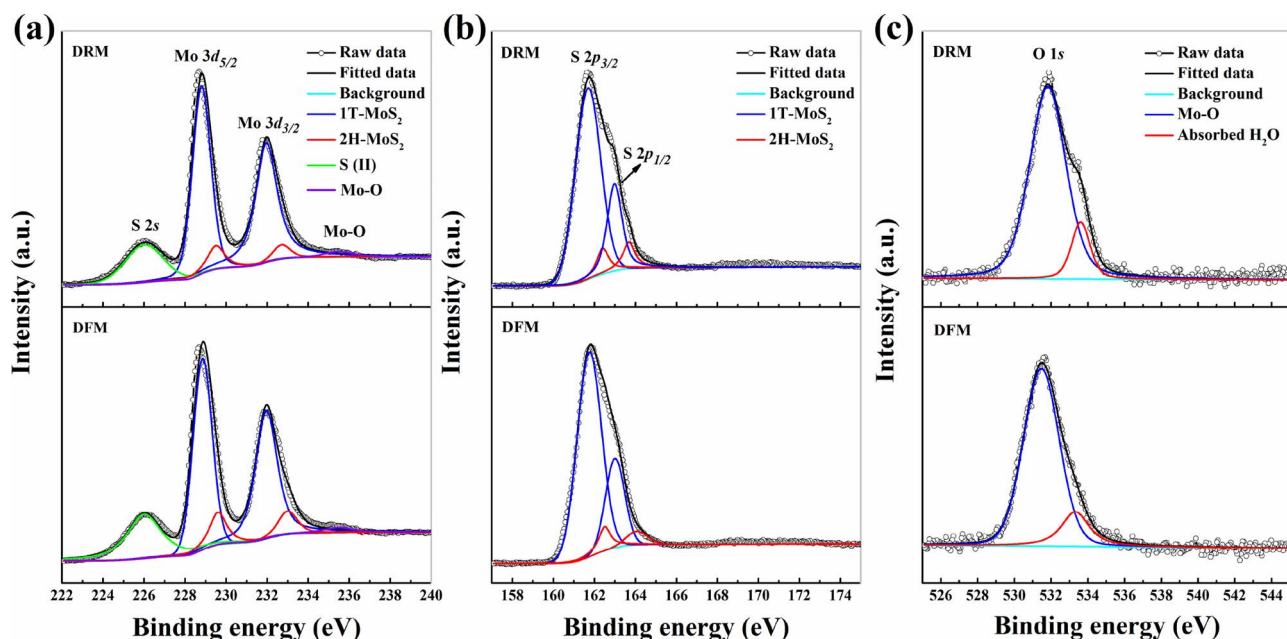
Fig. 2. High-resolution XPS spectra of (a) Mo 3d, (b) S 2p and (c) O 1s for DRM and DFM.

Raman spectra analysis is not only the powerful method to determine the phase of transition metal disulfides but also usually used to investigate the defects of the preformed catalysts. Fig. 4 shows that the Raman spectra of DRM and DFM are approximately the same. The strong peak at $146 \, cm^{-1}$ could be attributed to Mo-Mo stretching vibrations in $1T-MoS_2$ [52]. Not only that, the spectra at 236, 282, 335, $376 \, cm^{-1}$ and $402 \, cm^{-1}$ are also identified as the characteristic peak of $1T-MoS_2$ [57]. These results indicate that DRM and DFM both exhibit the 1T-phase octahedral prismatic structure. Besides, compared with DFM, DRM exhibits the relatively weaker peak intensity because of its weaker crystal structure intensity, also testifying the existence of intrinsic structural defects in DRM [43].

Additionally, the electrocatalytic activities of DRM and DFM were characterized by a series of electrochemical assays. The polarization curves showing the normalized current density versus voltage for DRM and DFM are shown in Fig. 5a. DRM displays a lower onset overpotential and a larger cathodic current density than DFM, demonstrating the superior electrocatalytic activity [30]. Besides, EIS was also
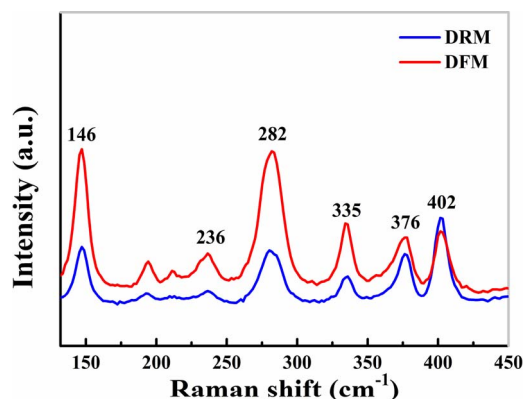

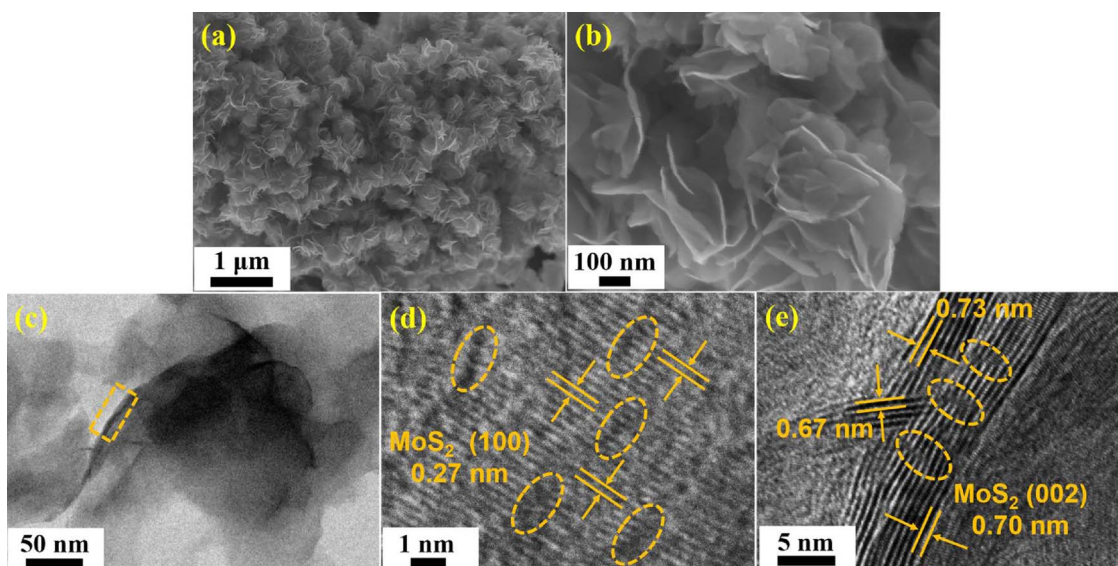**Fig. 4.** Roman shift of the DRM and DFM samples.

Fig. 3. (a, b) SEM and (c) TEM images of DRM sample. (d, e) HRTEM images of the selected sections marked in (c). The abundant defects are labelled by dashed circles.
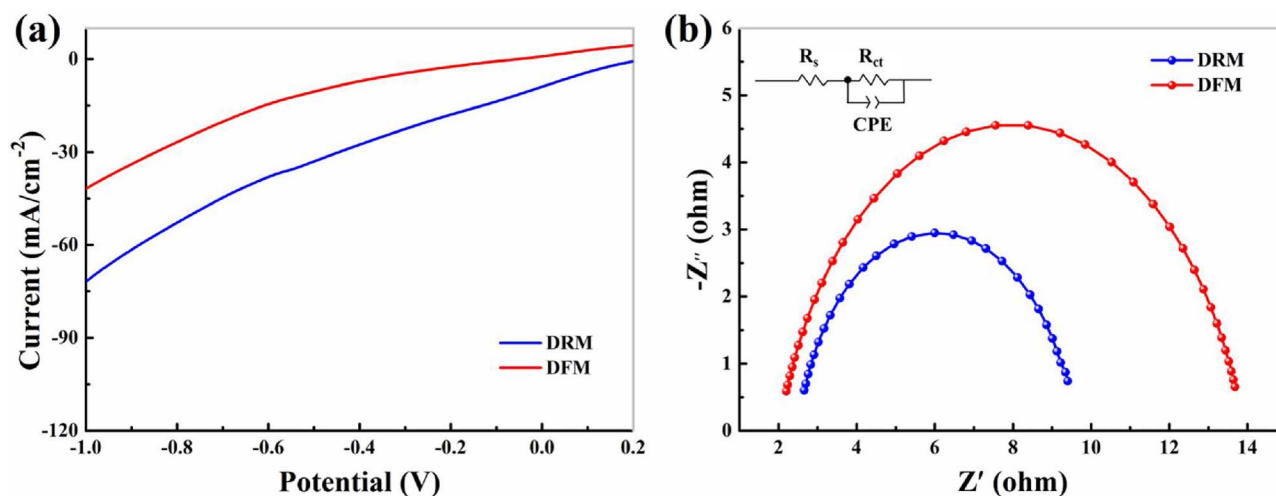
Fig. 5. Electrochemical measurements (a) I–V curves and (b) EIS Nyquist plots of as-prepared DRM and DFM samples.

conducted to provide further insight into the electrode kinetics during HER (Fig. 5b). Apparently, the Nyquist plots all showed semicircle features, and thus were fitted using a Randles equivalent circuit (inset in Fig. 5b) to extract the charge transfer resistance (R_{ct}). R_{ct} values of 7.1 and 11.9 Ω were obtained for DRM and DFM, respectively (Table S2). A smaller charge transfer resistance of DRM means better electron transport and more facile electrode kinetics during HER.

In order to more visually show the enrichment effect of the active site caused by the defects, the numbers of active sites for DRM and DFM samples were calculated according to the method in the literature [50]. We find that the density of active sites of DRM and DFM is 2.021×10^{-3} mol g^{-1} and 1.114×10^{-3} mol g^{-1}, respectively. Obviously, rich defects in DRM could give rise to enrichment effect of active sites, which are beneficial to the photocatalytic HER. Further, we employed EPR spectroscopy to provide fingerprint information for a paramagnetic signal to confirm the defects in DRM [53]. Following Fig. S4, the characteristic S signal at g factor of ~2.004 can be observed, and the intensity of DRM is lower than that of DFM due to the introduction of S vacancies as a format of defect in DRM [35,54]. Moreover, the FTIR spectrum (Fig. S5) indicates the complete removal of thiourea in DRM and DFM, namely, no thiourea molecules are adsorbed on the active edges [30,31].

3.2. Morphology, structure and optical property of hybrid catalysts

The crystalline structures of DRM-C nanohybrids with varying loadings of DRM (0, 10, 15, 20, 25, 30, 100 wt%) were further investigated by XRD. As shown in Fig. S6, the diffraction peaks of pure CdS and DRM-C heterostructures at 24.8°, 26.5°, 28.2°, 36.6°, 43.7°, 47.9° and 51.9° can be well-indexed to (100), (002), (101), (102), (110), (103) and (112) planes of hexagonal CdS (PDF#77-2306) [44]. When the DRM content in DRM-C is less than 20 wt%, no characteristic peaks of DRM occur because of a low loading and partial crystalline nature of DRM [55]. Further increasing DRM content up to 20 wt% or even more, the peaks at 9.0° and 33.0° assigned to DRM can be directly observed in DRM-C. Furthermore, we carried out measurements on the zeta potentials of DRM and CdS dispersed in deionized water, with values of -8.7 mV for DRM and 10.1 mV for CdS (Fig. S8), revealing the surface electrostatic interaction between CdS and DRM [41]. The morphology and microstructure of the as-prepared 20 wt% DRM-C heterostructure were further studied by SEM and TEM. As shown in Fig. 6a and b, CdS nanorods and flower-like DRM nanosheets are clearly discerned, indicating the successful preparation of DRM-C composite. In this heterostructure, CdS is composed of nanorods in a diameter of 40–50 nm and a length of several micrometers, which well agrees with

the pure CdS nanorods (Fig. S7a–c). Fig. 6c and d show the HRTEM of 20 wt% DRM-C sample, which display two fringes with interplanar spacings of 0.36 and 0.67 nm, corresponding to the (100) planes of hexagonal CdS and the (002) planes of DRM, respectively. It is worth noting that there are numerous defects in the DRM crystal matrix as labelled with dashed circles, which induce additional active edge sites and thus facilitate the improved photocatalytic HER [20]. Selected area electron diffraction (SAED) pattern as shown in the inset of Fig. 6c also indicates that the existence of CdS and MoS_2 crystal phases in the 20 wt% DRM-C heterostructure. In the SAED pattern of 20 wt% DRM-C, two sets of diffraction spots are observed, in which the inner spots correspond to CdS while the outer set belongs to MoS_2 [56,57]. Note that the SAED pattern appearing at 5.6 nm^{-1} shows the expected crystal symmetry for 1T-MoS_2 [57,58].

The EDS mapping (Fig. 7a–e) analysis of 20 wt% DRM-C sample also displays the uniform distribution of Cd, Mo and S, as well as the relatively weak signal of O in 20 wt% DRM-C, confirming that DRM is successfully loaded on the surface of CdS. Meanwhile, EDS spectra of 20 wt% DRM-C and 20 wt% DFM-C were also measured in parallel and the related results can be found in Fig. S9. UV–vis diffuse reflectance spectra measurement was also performed to study the optical property of samples [59]. As shown in Fig. 8a, the absorption edge for pure CdS is strictly confined at about 520 nm corresponding to its band gap energy of 2.42 eV; meanwhile, the DRM material shows a flat plot with a high adsorption coefficient throughout the UV–vis wavelength range, indicating that DRM exhibits a metallic character [21]. Furthermore, the absorption intensity of DRM-C heterostructures in visible light region from 520 to 800 nm enhance with the increase of DRM amount (10, 15, 20, 25, 30, 100 wt%), which is in accordance with the color change of samples from light yellow to greenish. Compared with pure CdS and 20 wt% DFM-C, 20 wt% DRM-C exhibits a higher adsorption intensity (Fig. 8b) beneficial to the photocatalytic HER activity and this will be discussed below. Besides, XPS data and analysis results show that DRM and DFM still contain approximately 81% 1T phase in composite heterostructures (Fig. S10).

3.3. Photocatalytic HER activities

The photocatalytic H_2 production rates of the samples were measured under visible light irradiation ($\lambda > 420$ nm) with lactic acid as sacrificial reagent, and the results are shown in Fig. 9. Fig. 9a shows the comparison of photocatalytic H_2 production activities of DRM, CdS, Pt/CdS, and DRM-C and DFM-C with different amounts of cocatalyst (10, 15, 20, 25, 30 wt%). It can be seen that almost no H_2 was detected when DRM alone was used as a photocatalyst, suggesting its very poor
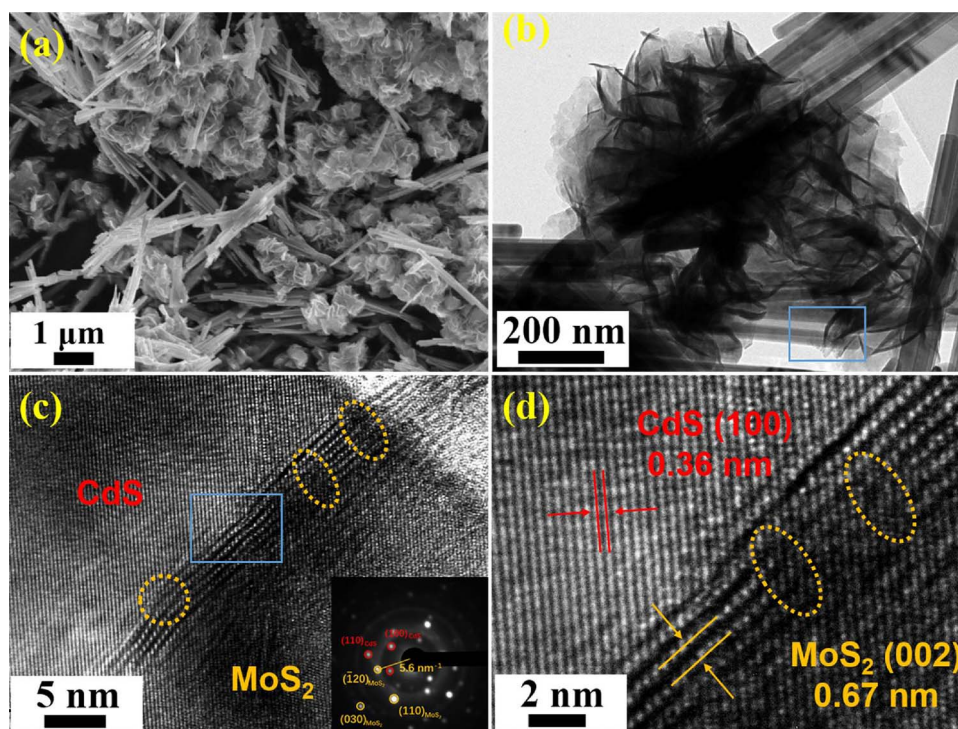
Fig. 6. (a, b) SEM and TEM images of 20 wt% DRM-C sample. (c) HRTEM image of the selected section marked in (b). The inset shows the corresponding SAED pattern of 20 wt% DRM-C sample. (d) HRTEM image of the selected section marked in (c).

photocatalytic HER activity. The pure CdS sample exhibits a very low photocatalytic H_2 production rate of 19.6 mmol h^{-1} g^{-1}, arising from its poor charge separation and transfer capability. When DRM or DFM was introduced onto CdS, the photocatalytic HER activity is significantly enhanced, and the rate of H_2 evolution increases with increasing DRM or DFM loading up to an optimum level of 20 wt%. However, further increasing the content of DRM or DFM in the

heterostructures will lead to a decrease of H_2 evolution activity probably due to the masking effect of MoS_2 [60,61]. Particularly, the photocatalytic HER activities of DRM-C increase markedly in comparison with those of DFM-C. Under optimized conditions, 20 wt% DRM-C shows the highest photocatalytic HER rate of 132.4 mmol h^{-1} g^{-1}, far higher than that of 20 wt% DFM-C (102.1 mmol h^{-1} g^{-1}). Meanwhile, such an extraordinary activity of 20 wt% DRM-C also far exceeds that of
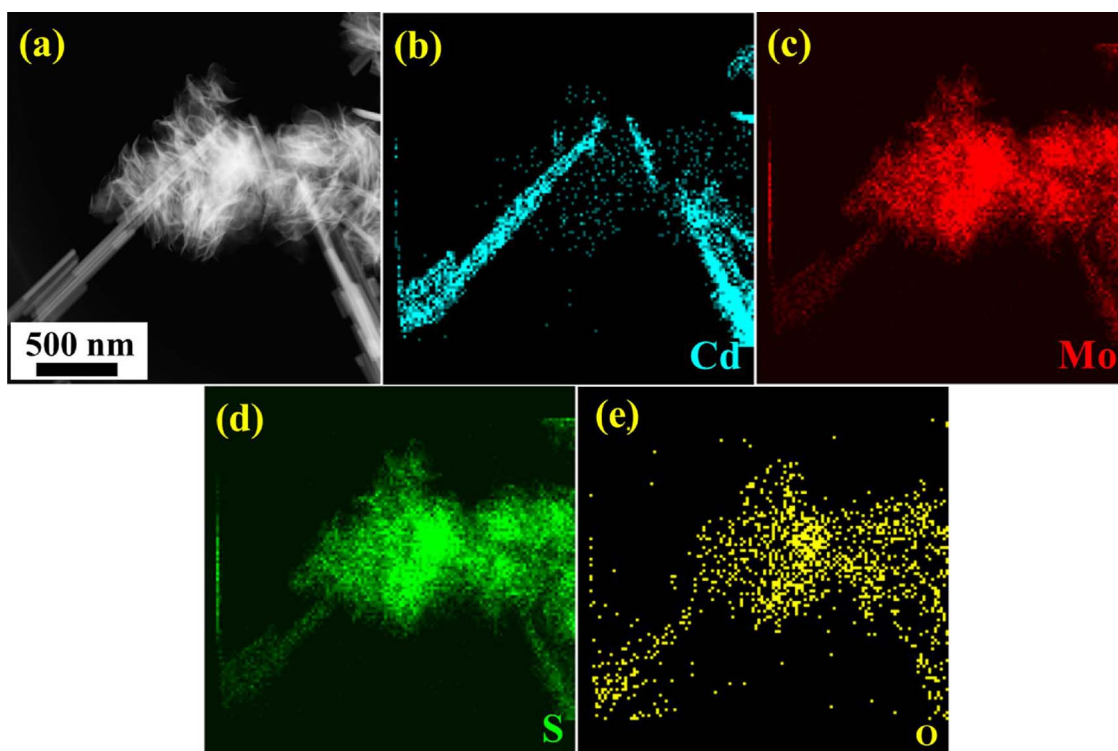

Fig. 7. (a) SEM image and (b–e) EDS elemental mapping of 20 wt% DRM-C heterostructure photocatalyst.
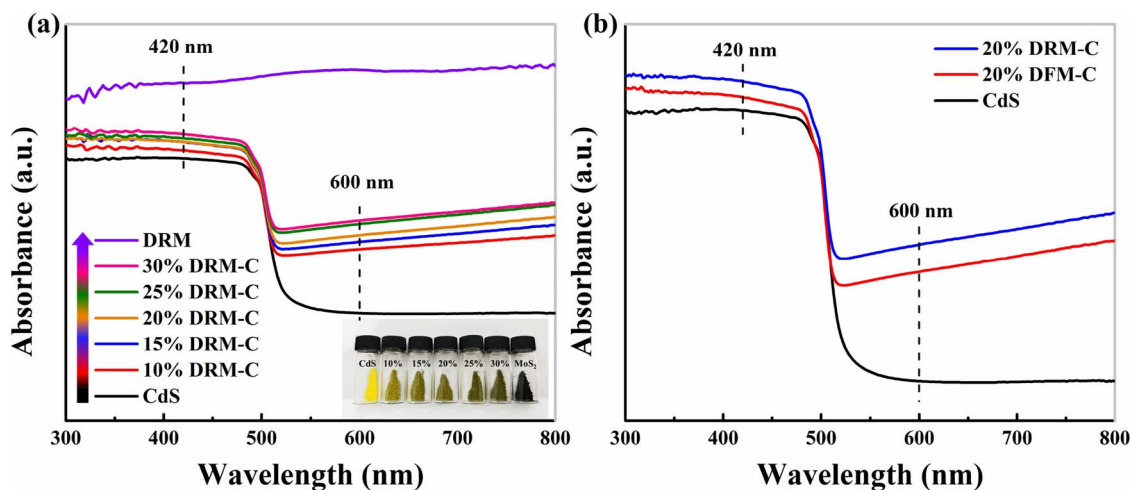
Fig. 8. (a) UV–vis light absorption spectra of DRM-C heterostructure photocatalysts containing different amounts of DRM (0, 10, 15, 20, 25, 30, 100 wt%). (b) UV–vis diffuse reflectance spectra of CdS, 20 wt% DRM-C and 20 wt% DFM-C.

pure CdS (20.0 mmol h^{-1} g^{-1}) and conventional Pt/CdS (89.0 mmol h^{-1} g^{-1}). As displayed in Fig. 9b, the AQY of 20 wt% DRM-C exposed in different regions of incident light wavelength are measured to be 47.0% at 420 nm and 4.0% at 460 nm, which are both higher than that of 20 wt% DFM-C (20.7% at 420 nm; 2.3% at 460 nm). The stability assays (Fig. 9c) show that after four runs 20 wt% DRM-C and 20 wt% DFM-C both possess good catalytic stability and the photocatalytic HER activity of the former is obviously higher than that of the latter. Additionally, we carried out photocatalytic H$_2$ production catalyzed by 20 wt% DRM-

C under a prolonged visible light irradiation (λ > 420 nm) of 30 h (Fig. 9d). No obvious decay of photocatalytic HER was observed, suggesting its durability and practical application.

3.4. Origin of the enhanced performance

To explore the reasons of the significantly enhance photocatalytic HER over the DRM-C photocatalyst, we then performed a series of careful characterizations for blank CdS, DRM-C and DFM-C samples.
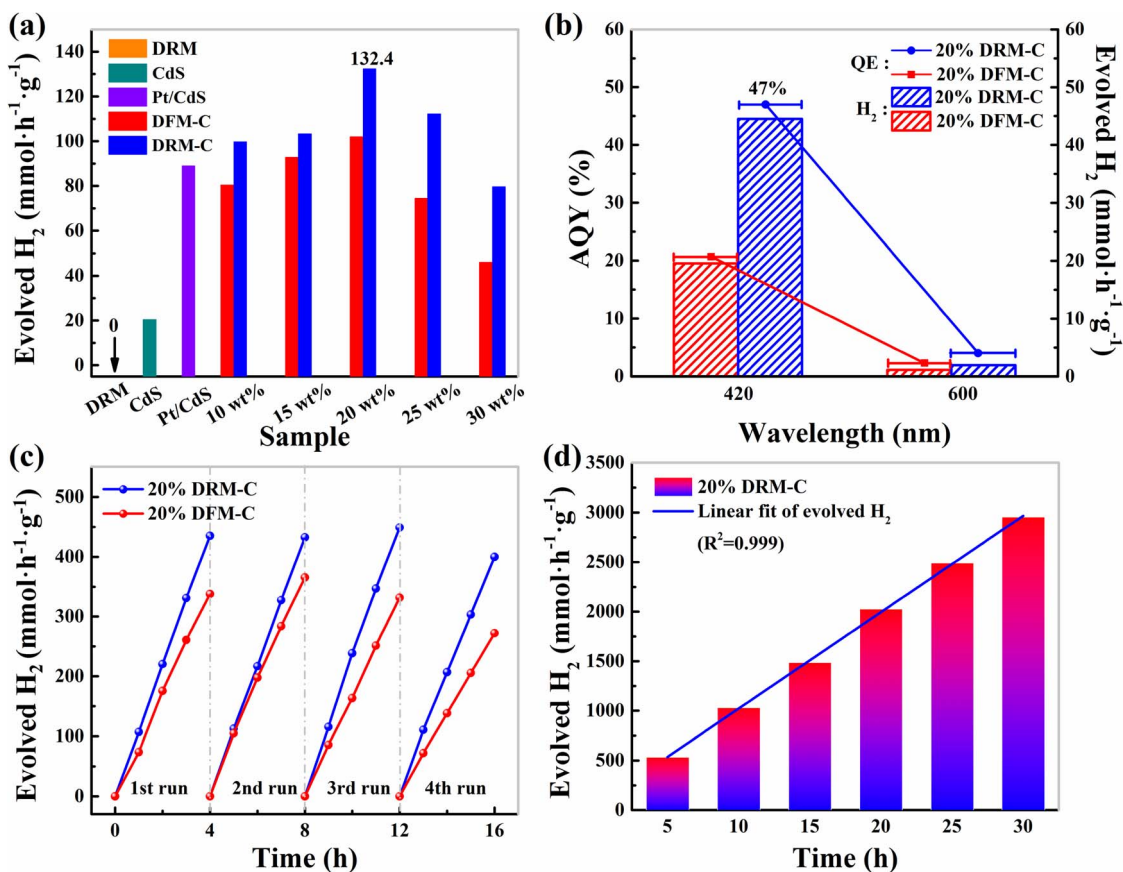

Fig. 9. (a) Photocatalytic H$_2$ evolution rates for DRM, CdS, Pt/CdS, and DRM-C and DFM-C containing different amounts of cocatalyst (10, 15, 20, 25, 30 wt%) under visible light irradiation. (b) Wavelength-dependent AQY and hydrogen evolution from water by 20 wt% DRM-C and 20 wt% DFM-C. (c) Cyclic H$_2$ production on 20 wt% DRM-C and 20 wt% DFM-C. (d) Photocatalytic H$_2$ production catalyzed by 20 wt% DRM-C under a prolonged visible light irradiation of 30 h. Conditions: 2 mg CdS, 20 mL aqueous solution with 2 mL lactic acid and 500 W metal halide lamp with an optical cutoff filter (λ > 420 nm).
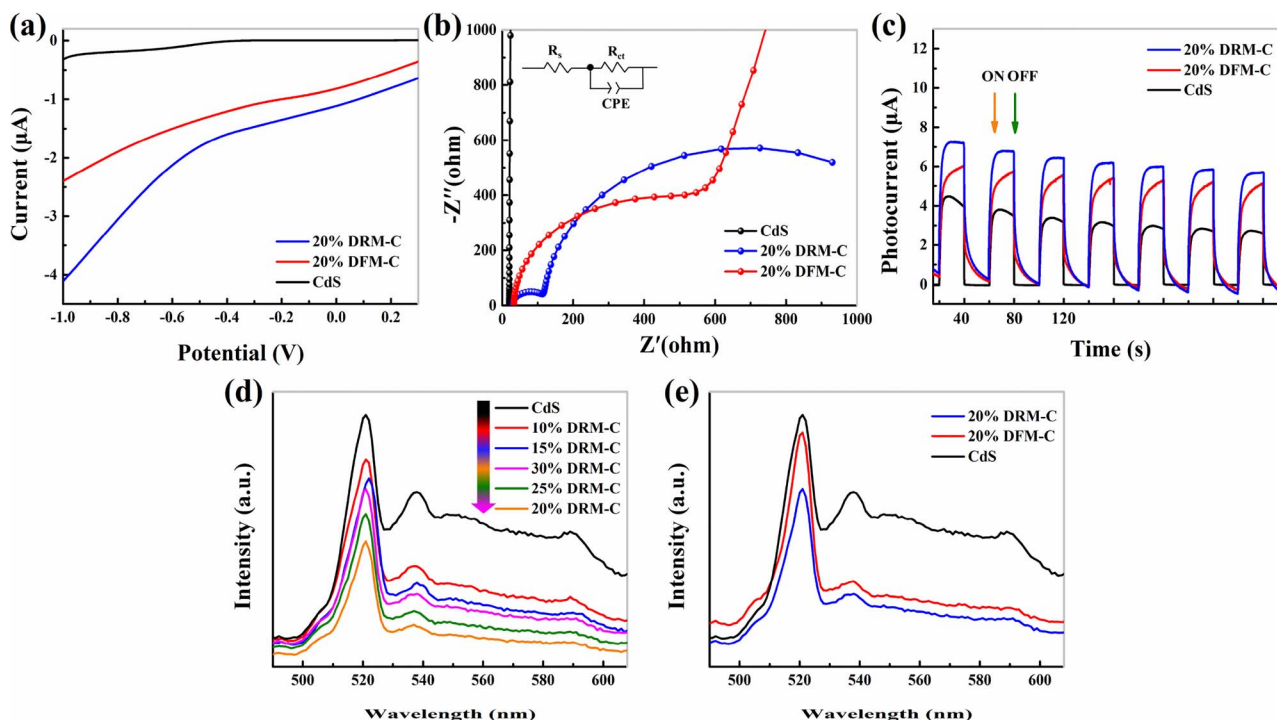
Fig. 10. (a) I–V curves, (b) EIS Nyquist plots and (c) visible light ($\lambda > 420$ nm) induced transient photocurrent responses of pure CdS, 20 wt% DFM-C and 20 wt% DRM-C. (d) PL spectra of DRM-C photocatalysts containing different amounts of DRM (0, 10, 15, 20, 25, 30, 100 wt%). (e) PL spectra of CdS, 20 wt% DFM-C and 20 wt% DRM-C.

The photoelectrochemical performance is widely considered to be an efficient evidence for confirming the electron-hole pair separation and transfer in the composite photocatalysts, including the transient photocurrent responses, EIS and I–V. Fig. 10a shows the polarization curves of samples. Compared with pure CdS and 20 wt% DFM-C, 20 wt% DRM-C displays an enhanced current density, indicating that DRM can efficiently promote the photoactivity of reduction of water to H_2 [50]. The diagrams of the arc radius on the EIS Nyquist plots of pure CdS and 20 wt% DFM-C, 20 wt% DRM-C are shown in Fig. 10b. The semicircles can be simulated well by an electrical equivalent circuit diagram (inset in Fig. 10b) and the corresponding fitted values of three samples are shown in Table S2. It can be clearly seen that the charge R_{ct} of 20 wt% DRM-C (104.1 Ω) is smaller than that of 20 wt% DFM-C (579.3 Ω), also far smaller than that of pure CdS (32150 Ω), indicating efficient interfacial charge-carrier separation and transfer in the DRM-C heterostructure [62,63]. Fig. 10c shows the photocurrent density of the three composites with 20 s under visible light irradiation on/off cycles. Apparently, the photocurrent of 20 wt% DRM-C is superior to that of pure CdS and 20 wt% DFM-C, suggesting that the DRM-C heterostructure has the best performance for generating and suppressing the recombination of photoinduced charge carriers [20]. Moreover, the photocurrent responses were highly reproducible for several on-off cycles and remained stable.

Further, PL emission spectra technology is also considered to be a powerful tool to characterize the radiative recombination process of photo-excited charge carriers in the samples. The PL spectra of photocatalysts were measured at 426 nm excitation (Fig. S11). Fig. 10d presents the fluorescence spectra of pure CdS and DRM-C with different DRM loading contents. The broad fluorescence peaks of all samples appearing at ~520 nm can be assigned to near-band-edge emission of CdS [64]. The peak at ~538 nm is believed to be associated with structural defects arisen from the core defects on the CdS nanorods surfaces [64]. The PL spectrum at ~590 nm can be ascribed to a band-to-band emission of CdS [65]. Pure CdS shows the strongest emission due to the high recombination of photoexcited charges. The emissions were remarkably quenched upon loading DRM, attributing to the fast transfer of electrons from CdS to DRM [66], which can suppress the

electron-hole recombination of CdS and enhance the photocatalytic activity. Especially, the PL intensity of 20 wt% DRM-C is lowest among a series of DRM-C catalysts, corresponding to the optimal H_2 evolution activity. Moreover, Fig. 10e presents the comparison of PL emission spectra of pure CdS, 20 wt% DFM-C and 20 wt% DRM-C samples. Notably, 20 wt% DRM-C exhibits greater quenched PL signals than the other catalysts, indicating a more efficient charge separation in good agreement with the photoelectrochemical analyses [55].

To verify the relative positions of conduction band (CB) and valence band (VB) of samples, Mott-Schottky plots and XPS valence band spectra were also measured. In general, the flat-band potential can be used to approximately estimate the CB position [67]. Based on the plots shown in Fig. 11a–c, the flat band potentials are estimated to be -0.5 eV, -0.4 eV and -0.3 eV vs. SCE for CdS, DFM and DRM, respectively. In addition, according to the XPS valence-band spectra (Fig. S12), the VB positions of DFM and DFM are all determined as 0 eV vs. NHE, indicating that DRM and DFM belong to metallic phase [21,47]. According to the above data and analysis, the band structure of the photocatalysts can be depicted in Fig. 11d. Obviously, the CB potential of DRM has a positive shift of 0.1 eV compared with DFM. According to the H_2 evolution "band matching" theory [68], the photo-excited electrons from CdS would be easier to be injected into the CB of DRM because of lower and favorable energy level of DRM. This sketch could help decipher the reasons behind the difference between DRM and DFM loading on CdS in relation to their catalytic hydrogen activities. Besides, the photocatalytic HER process of DRM-C heterostructure under the visible-light irradiation is schematically displayed in Fig. 11e. Typically, under visible light illumination, electron-hole pairs are generated in CdS nanorods. The photo-excited electrons readily transfer to DRM cocatalyst and then reduce H^+ to H_2, accompanied by the consumption of the holes by reacting with the sacrificial agent of lactic acid, achieving the fast transfer and separation of charge carriers.

4. Conclusions

Defect-rich and defect-free O-incorporated $1T$-MoS_2 nanosheets i.e. DRM and DFM were successfully synthesized and subsequently used as
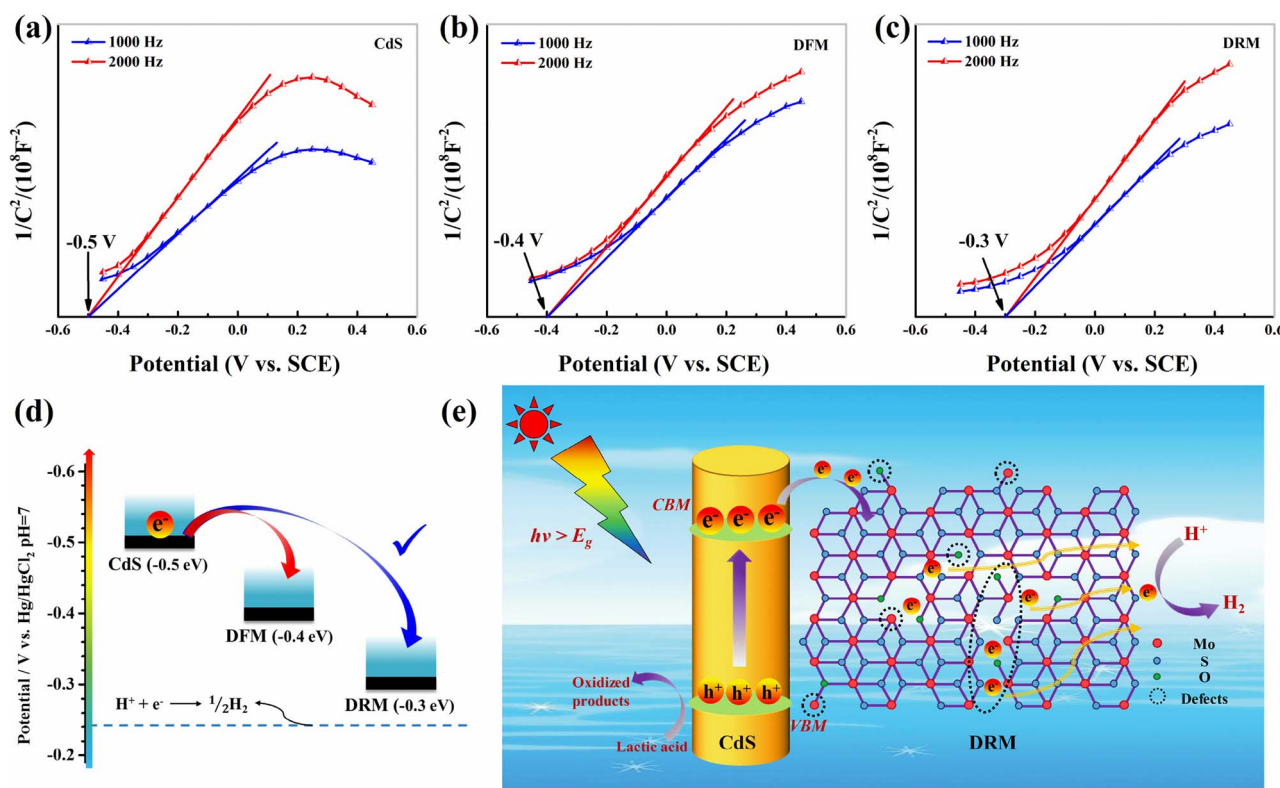
Fig. 11. (a–c) Mott-Schottky plots of CdS, DFM and DRM. (d) Schematic illustration of the band structure of CdS, DFM and DRM. (e) Schematic illustration of the photogenerated charge transfer in the DRM-C heterostructure under visible light irradiation ($\lambda > 420$ nm).

effective cocatalysts for visible-light photocatalytic H_2 evolution over CdS nanorods. With the merits of the defect-induced additional active sites as well as the suitable CB potential of DRM relative to DFM, DRM-C exhibits excellent photocatalytic HER activity. Specifically, under an optimized DRM/CdS ratio of 20 wt%, DRM-C achieves a remarkable enhanced visible light ($\lambda > 420$ nm) photocatalytic H_2 production rate of 132.4 mmol h^{-1} g^{-1}, which is obviously higher than that of 20 wt% DFM-C, and also far higher than that of pure CdS and commonly-used Pt/CdS. These findings provide more opportunities for the development of structure- and phase-engineered transition metal dichalcogenides for high-efficiency visible-light or solar photocatalysts applied in various fields.

Acknowledgement

Appendix A. Supplementary data

Supplementary material related to this article can be found, in the online version, at doi:https://doi.org/10.1016/j.apcatb.2018.02.025.

References

[1] H. Zhang, G. Liu, L. Shi, H. Liu, T. Wang, J. Ye, Nano Energy 22 (2016) 149–168.
[2] A. Kudo, Y. Miseki, Chem. Soc. Rev. 38 (2009) 253–278.
[3] A.J. Esswein, D.G. Nocera, Chem. Rev. 107 (2007) 4022–4047.
[4] X. Chen, S. Shen, L. Guo, S.S. Mao, Chem. Rev. 110 (2010) 6503–6570.
[5] J. Chen, X.J. Wu, L. Yin, B. Li, X. Hong, Z. Fan, B. Chen, C. Xue, H. Zhang, Angew. Chem. 54 (2015) 1210–1214.
[6] T. Simon, N. Bouchonville, M.J. Berr, A. Vaneski, A. Adrović, D. Volbers, R. Wyrwich, M. Döblinger, A.S. Susha, A.L. Rogach, Nat. Mater. 13 (2014) 1013–1018.
[7] M.B. Wilker, K.E. Shinopoulos, K.A. Brown, D.W. Mulder, P.W. King, G. Dukovic, J. Am. Chem. Soc. 136 (2014) 4316–4324.
[8] Y. Li, Y. Hu, S. Peng, G. Lu, S. Li, J. Phys. Chem. C 113 (2009) 9352–9358.
[9] Y. Li, L. Tang, S. Peng, Z. Li, G. Lu, CrystEngComm 14 (2012) 6974–6982.
[10] K. Wu, Y. Du, H. Tang, Z. Chen, T. Lian, J. Am. Chem. Soc. 137 (2015) 10224–10230.
[11] R. Marschall, Adv. Funct. Mater. 24 (2014) 2421–2440.
[12] F.E. Osterloh, Cheminform 39 (2008) 35–54.
[13] Y. Li, D. Gao, S. Peng, G. Lu, S. Li, Int. J. Hydrogen Energy 36 (2011) 4291–4297.
[14] J. Ran, G. Gao, F.-T. Li, T.-Y. Ma, A. Du, S.-Z. Qiao, Nat. Commun. 8 (2017) 13907–13916.
[15] W.-F. Chen, J.T. Muckerman, E. Fujita, Chem. Commun. 49 (2013) 8896–8909.
[16] S. Carenco, D. Portehault, C. Boissiere, N. Mezailles, C. Sanchez, Chem. Rev. 113 (2013) 7981–8065.
[17] G. Zhang, H. Liu, J. Qu, J. Li, Energy Environ. Sci. 9 (2016) 1190–1209.
[18] Q. Lu, Y. Yu, Q. Ma, B. Chen, H. Zhang, Adv. Mater. 28 (2016) 1917–1933.
[19] X. Cao, C. Tan, X. Zhang, W. Zhao, H. Zhang, Adv. Mater. 28 (2016) 6167–6196.
[20] K. Chang, X. Hai, J. Ye, Adv. Energy Mater. 6 (2016) 10033–10041.
[21] Q. Yue, Y. Wan, Z. Sun, X. Wu, Y. Yuan, P. Du, J. Mater. Chem. A 3 (2015) 16941–16947.
[22] L. Feng, F. Song, X. Hu, Energy Environ. Sci. 8 (2015) 2347–2351.
[23] Y. Liu, X. Hua, C. Xiao, T. Zhou, P. Huang, Z. Guo, B. Pan, Y. Xie, J. Am. Chem. Soc. 138 (2016) 5087–5092.
[24] M. Caban-Acevedo, M.L. Stone, J.R. Schmidt, J.G. Thomas, Q. Ding, H.C. Chang, M.L. Tsai, J.H. He, S. Jin, Nat. Mater. 14 (2015) 1245–1251.
[25] Q. Tang, D.-e. Jiang, ACS Catal. 6 (2016) 4953–4961.
[26] T.F. Jaramillo, K.P. JøRgensen, J. Bonde, J.H. Nielsen, S. Horch, I. Chorkendorff, Science 317 (2007) 100–102.
[27] G. Gao, Y. Jiao, F. Ma, Y. Jiao, E. Waclawik, A. Du, J. Phys. Chem. C 119 (2015) 13124–13128.
[28] J. Xu, Y. Li, S. Peng, Int. J. Hydrogen Energy 40 (2015) 353–362.
[29] Y. Li, H. Wang, S. Peng, J. Phys. Chem. C 118 (2014) 19842–19848.
[30] J. Xie, H. Zhang, S. Li, R. Wang, X. Sun, M. Zhou, J. Zhou, X.W.D. Lou, Y. Xie, Adv. Mater. 25 (2013) 5807–5813.
[31] J. Xie, J. Zhang, S. Li, F. Grote, X. Zhang, H. Zhang, R. Wang, Y. Lei, B. Pan, Y. Xie, J. Am. Chem. Soc. 135 (2013) 17881–17888.
[32] Y. Guo, X. Zhang, X. Zhang, T. You, J. Mater. Chem. A 3 (2015) 15927–15934.
[33] J. Xie, J. Xin, G. Cui, X. Zhang, L. Zhou, Y. Wang, W. Liu, C. Wang, M. Ning, X. Xia, Inorg. Chem. Front. 3 (2016) 1160–1166.
[34] G. Ye, Y. Gong, J. Lin, B. Li, Y. He, S.T. Pantelides, W. Zhou, R. Vajtai, P.M. Ajayan, Nano Lett. 16 (2016) 1097–1103.
[35] Y. Yin, J. Han, Y. Zhang, X. Zhang, P. Xu, Q. Yuan, L. Samad, X. Wang, Y. Wang, Z. Zhang, J. Am. Chem. Soc. 138 (2016) 7965–7972.
[36] D. Kong, H. Wang, J.J. Cha, M. Pasta, K.J. Koski, J. Yao, Y. Cui, Nano Lett. 13 (2013) 1341–1347.
[37] J. Kibsgaard, Z. Chen, B.N. Reinecke, T.F. Jaramillo, Nat. Mater. 11 (2012) 963–969.

[38] D. Merki, S. Fierro, H. Vrubel, X. Hu, Chem. Sci. 2 (2011) 1262–1267.
[39] Y.H. Chang, C.T. Lin, T.Y. Chen, C.L. Hsu, Y.H. Lee, W. Zhang, K.H. Wei, L.J. Li, Adv. Mater. 25 (2013) 756–760.
[40] Y.-H. Chang, R.D. Nikam, C.-T. Lin, J.-K. Huang, C.-C. Tseng, C.-L. Hsu, C.-C. Cheng, C.-Y. Su, L.-J. Li, D.H. Chua, ACS Appl. Mater. Interfaces 6 (2014) 17679–17685.
[41] J. Xiong, Y. Liu, D. Wang, S. Liang, W. Wu, L. Wu, J. Mater. Chem. A 3 (2015) 12631–12635.
[42] H. Lin, Y. Li, H. Li, X. Wang, Nano Res. 10 (2017) 1377–1392.
[43] Q. Liu, Q. Shang, A. Khalil, Q. Fang, S. Chen, Q. He, T. Xiang, D. Liu, Q. Zhang, Y. Luo, ChemCatChem 8 (2016) 2614–2619.
[44] Z. Sun, H. Zheng, J. Li, P. Du, Energy Environ. Sci. 8 (2015) 2668–2676.
[45] R. Peng, L. Liang, Z.D. Hood, A. Boulesbaa, A. Puretzky, A.V. Ievlev, J. Come, O.S. Ovchinnikova, H. Wang, C. Ma, ACS Catal. 6 (2016) 6723–6729.
[46] Q. Liu, X. Li, Q. He, A. Khalil, D. Liu, T. Xiang, X. Wu, L. Song, Small 11 (2015) 5556–5564.
[47] K. Chang, X. Hai, H. Pang, H. Zhang, L. Shi, G. Liu, H. Liu, G. Zhao, M. Li, J. Ye, Adv. Mater. 28 (2016) 10033–10041.
[48] G. Eda, H. Yamaguchi, D. Voiry, T. Fujita, M. Chen, M. Chhowalla, Nano Lett. 11 (2011) 5111–5116.
[49] C.A. Papageorgopoulos, W. Jaegermann, Surf. Sci. 338 (1995) 83–93.
[50] Y. Sun, X. Hu, W. Luo, Y. Huang, ACS Nano 5 (2011) 7100–7107.
[51] D.A. Reddy, J. Choi, S. Lee, Y. Kim, S. Hong, D.P. Kumar, T.K. Kim, Catal. Sci. Technol. 6 (2016) 6197–6206.
[52] S.J. Sandoval, D. Yang, R. Frindt, J. Irwin, Phys. Rev. B 44 (1991) 3955.
[53] J. Xu, Y. Teng, F. Teng, Sci. Rep. 6 (2016) 32457–32465.
[54] L. Wang, X. Liu, J. Luo, X. Duan, J. Crittenden, C. Liu, S. Zhang, Y. Pei, Y. Zeng, Angew. Chem. Int. Ed. 56 (2017) 7610–7614.
[55] X.-L. Yin, L.-L. Li, W.-J. Jiang, Y. Zhang, X. Zhang, L.-J. Wan, J.-S. Hu, ACS Appl. Mater. Interfaces 8 (2016) 15258–15266.
[56] W. Zheng, W. Feng, X. Zhang, X. Chen, G. Liu, Y. Qiu, T. Hasan, P. Tan, P.A. Hu, Adv. Funct. Mater. 26 (2016) 2648–2654.
[57] M.A. Lukowski, A.S. Daniel, F. Meng, A. Forticaux, L. Li, S. Jin, J. Am. Chem. Soc. 135 (2013) 10274–10277.
[58] L. Jiang, S. Zhang, S.A. Kulinich, X. Song, J. Zhu, X. Wang, H. Zeng, Mater. Res. Lett. 3 (2015) 177–183.
[59] Y. Li, Y. Hou, Q. Fu, S. Peng, Y.H. Hu, Appl. Catal. B: Environ. 206 (2017) 726–733.
[60] L. Shen, M. Luo, Y. Liu, R. Liang, F. Jing, L. Wu, Appl. Catal. B: Environ. 166–167 (2015) 445–453.
[61] Y.J. Yuan, F. Wang, B. Hu, H.W. Lu, Z.T. Yu, Z.G. Zou, Dalton Trans. 44 (2015) 10997–11003.
[62] L. Yang, Q. Xu, F. Teng, D. Yu, Y. Yang, W. Gu, Y. Teng, J. Xu, Y. Guo, Appl. Catal. B: Environ. 202 (2017) 355–363.
[63] F. Ma, Y. Wu, Y. Shao, Y. Zhong, J. Lv, X. Hao, Nano Energy 27 (2016) 466–474.
[64] S. Liu, N. Zhang, Z.-R. Tang, Y.-J. Xu, ACS Appl. Mater. Interfaces 4 (2012) 6378–6385.
[65] B. Chai, M. Xu, J. Yan, Z. Ren, Appl. Surf. Sci. 430 (2018) 523–530.
[66] T.T. Zhuang, Y. Liu, M. Sun, S.L. Jiang, M.W. Zhang, X.C. Wang, Q. Zhang, J. Jiang, S.H. Yu, Angew. Chem. 54 (2015) 11495–11500.
[67] G.F. Long, X.H. Li, K. Wan, Z.X. Liang, J.H. Piao, P. Tsiakaras, Appl. Catal. B: Environ. 203 (2017) 541–548.
[68] B. Qiu, Q. Zhu, M. Xing, J. Zhang, Chem. Commun. 53 (2017) 897–900.